INERTIAL CONFINEMENT FUSION

TECHNICAL REVIEW

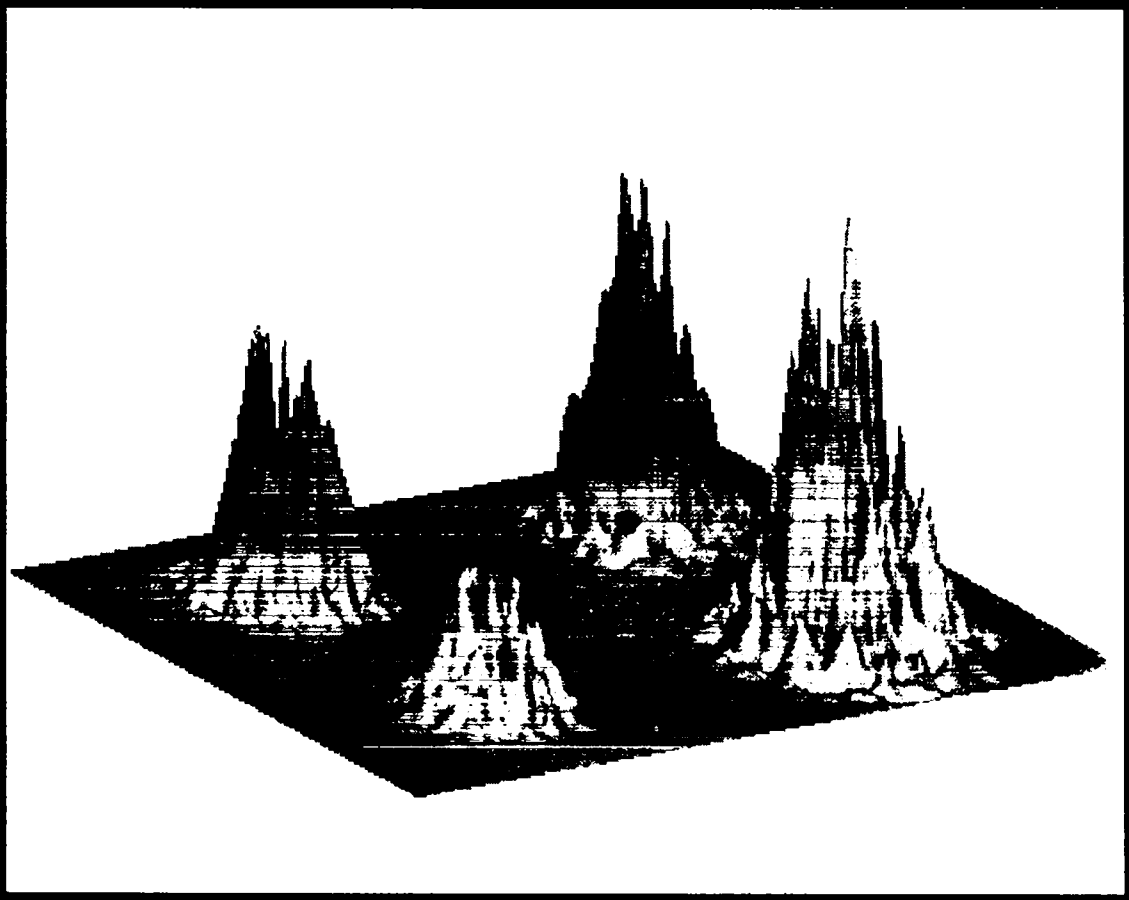

LOS ALAMOS

January 1992
Volume 1

Front Cover

Simulated GXI: Test images for symmetry legendre analysis.
Provided by David Gold, P-4.

"Do you not reflect that it will be possible for a person ...

when he sees the beautiful with the mind ...

to give birth ... to realities?"

Plato

Policy on ES&H

Implicit in all of our work is a respect for the health and safety of ourselves and those around us and an appreciation for the need to protect the environment in which we are privileged to work.

Spatially Discriminating Optically Streaked Spectrograph (SDOSS)

For further information on this subject contact:

John A. Oertel

Camilo Gomez

Juan Fernandez

Scott Evans

Los Alamos
National Laboratory
Los Alamos, NM 87545

The Laser-Matter Interaction and Fusion Physics Group (P-4) at Los Alamos National Laboratory has recently designed and is implementing a temporally and spectrally resolved optical diagnostic to be permanently operated on the NOVA laser target chamber. SDOSS is designed to measure Stimulated Raman Scattering (SRS), which may be used to infer plasma densities. The SRS spectrum is also of interest to laser fusion because the instability decreases drive efficiency. SDOSS can view discrete target regions 200 μm in diameter, resolve events better than 300 ps, detect wavelengths between 300 nm and 1300 nm, and observe spectral windows up to 900 nm wide. These attributes set SDOSS apart from all other spectrally streaked diagnostics at NOVA.

Initially, SDOSS will be used to infer plasma densities from the SRS spectrum. Under certain conditions in plasmas with sub-quarter-critical densities, there is a one-to-one correspondence between the local electron density and the scattered SRS wavelength. A coarse measurement of the peak interaction density can be made using an SRS diagnostic with spatial discrimination. This type of diagnostic is useful in target configurations in which conventional density diagnostics (probing, spectroscopy) may be difficult or impossible to implement.

Technical Review

CCD camera having 58 pixels/mm (H) and 75 pixels/mm (V). The CCD is interfaced to a high-resolution image monitor and a 386 based computer via a GPIB data link. Data acquisition is managed by a commercial Temporal Analyzer software package that has a variety of data analyzing functions. Image files are saved in ASCII or binary and are archived on 44 Mb Bernoulli disks.

Wheras the overall sensitivity of SDOSS depends upon how well light is coupled into the fiberoptic taper, the spectral efficiencies of SDOSS components are shown in Figure 2. Important components are mirror coatings, diffraction gratings, the fiber optic cable, and the streak camera photocathode. Because most fiber optic cables were designed for commun-ion service, they typically have inadequate transmissions at wavelengths below 850 nm. However, by using a short 10-meter fiber, the effective attenuation becomes negligible over the wavelengths of interest. The gratings installed in the spectrometer are 100 g/mm with 600 nm blaze, 300 g/mm with 500 nm blaze, and 600 g/nm with 500 nm blaze. In most cases the upper and lower limits on the wavelength sensitivity are set by the diffraction grating, but these limits are dependent upon the selected grating. Excluding the grating, the dominant limitation is the streak camera's photocathode with a spectral sensitivity between 300 nm and 1300 nm. We also have an alternate streak camera with a S-20 photocathode that has superior sensitivity in the UV compared to the S-1. The temporal dispersion of SDOSS is dominated by the dispersion in

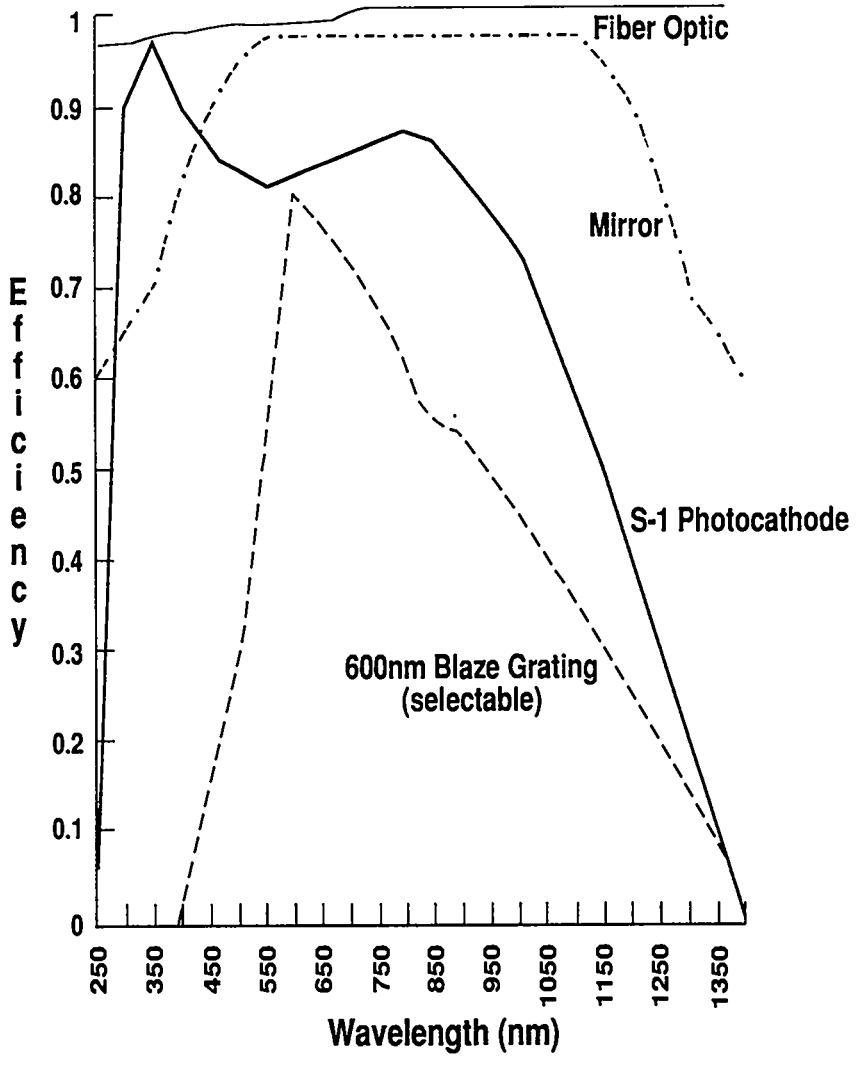

Fig. 2. Spectral efficiency of SDOSS.

the fiber optic cable, which at 850-nm wavelength and a cable length of 10 m is 300 ps, as verified experimentally. Spectral resolution is limited by the streak camera; for the various gratings this becomes, 3.64 nm, 1.21 nm, and 0.61 nm for the 100 g/mm, and 600 g/mm, respectively. ■

A Simplified Model for Designing Large KrF Amplifiers

For further information on this subject contact:

J. Al Sullivan

Los Alamos
National Laboratory
Los Alamos, NM 87545

Abstract

A simplified model for determining the performance of large krypton fluoride laser amplifiers is presented. The model includes a straightforward treatment of the controlling kinetics, an exact solution for energy extraction, and an approximation to amplified spontaneous emission losses; it can be easily programmed to run on personal computers. The inclusion of the controlling basic physics for KrF lasers makes the model ideally suited for the many calculations that are necessary to optimize the design of a specific amplifier. The basic parameters determined in the model are compared to experimental data wherever possible, and the large amplifier performance predictions are compared to the results from the most sophisticated kinetics and a three-dimensional extraction model that includes a full treatment of losses due to amplified spontaneous emission.

Introduction

The design of large inertial confinement fusion (ICF) and inertial fusion energy (IFE) drivers using KrF lasers requires estimates of the size and performance of the power amplifiers to be used. The power amplifiers are defined here as the last two stages in the amplification chain and they make up most of the cost for the amplification chain. Future designs for ICF facilities contain ultimate amplifiers that deliver as much as 500 kJ from a single amplifier and penultimate amplifiers

as large as 150-kJ output energy. For design purposes, accurate and rapid estimates of performance are desirable due to the iterative nature of the driver design process. In view of this, simplified codes that include all of the important physics are highly desirable. To achieve accuracy, simplified codes must include the dominant physics of extraction and the most important aspects of gain generation and depletion. Such codes are normally short enough to run rapidly on personal computers. Estimates of the small signal gain (g_o), the nonsaturable absorption (α), the saturation intensity (I_{sat}), and the formation efficiency are needed. In addition, an estimate of the losses due to amplified spontaneous emission (ASE) and the losses due to vignetting of extraction beams in angular multiplexed laser architectures is needed.

An alternate approach to the design of KrF amplifiers is to develop and use complex computer codes that are models of the full kinetics and three-dimensional aspects of ASE. Such codes require knowledge of the full set of over one hundred rate constants and significant computer capability to calculate ASE losses. At the present time, the required rate constants are not well known and there is no consistent set of experimental data for g_o, α, and I_{sat} that would permit confident bench marking of these sophisticated codes.

In the material that follows, the elements that make up a useful design code for electron-beam-pumped KrF amplifiers will be explained.

Determination of Laser Parameters (g_o, α, I_{sat})

Consider a dual-pass amplifier that can be represented schematically as shown in Fig. 1. The extracting flux enters from the right, passes through the laser media, and is turned back upon

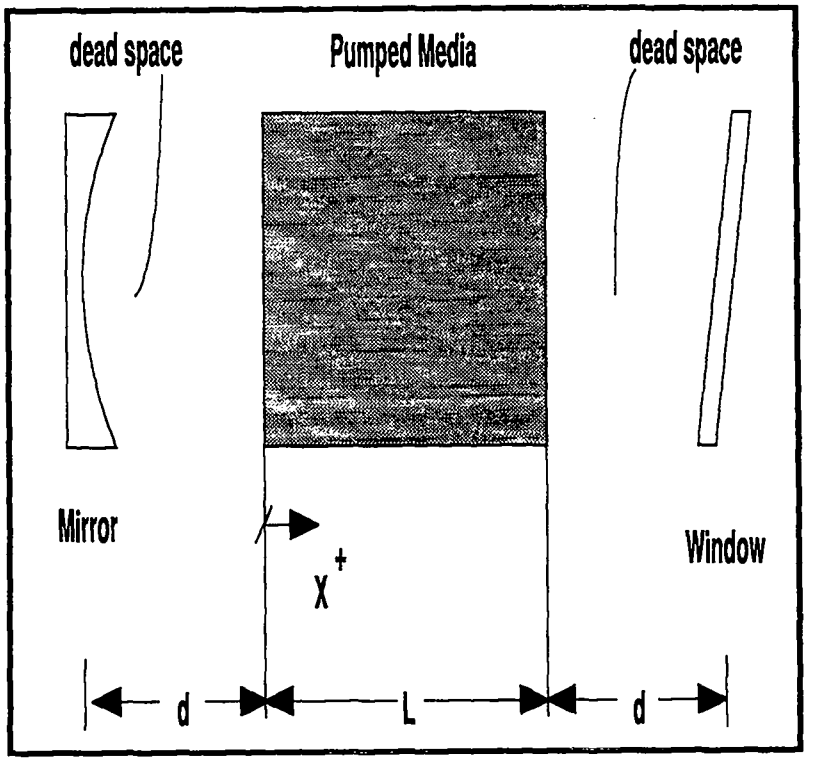

Fig. 1. Shown are the elements of the dual-pass amplifier model. The model includes mirror and window losses, as well as losses due to absorption in the unpumped end zones and in the pumped media.

itself to pass through the laser media a second time before it exits through the window. The laser media is bounded on each end by unpumped zones that are used to protect the mirror and window from pumping electrons and from the atomic fluorine in the pumped volume. Rice et al.[1] have shown that the differential equations governing the growth of the intensity of an extracting beam as a function of the spatial coordinate is given by

$$\pm \frac{dI_{\pm}}{dx} = I_{\pm}(g - \alpha) \quad , \tag{1}$$

where I is the intensity (w/cm^2), g is the loaded gain

$$g = \frac{g_o}{1 + \frac{(I_+ + I_-)}{I_{sat}}} \quad , \tag{2}$$

and α is the nonsaturable absorption. In Eq. (2) the symbol g_o is used for the unloaded amplifier gain. The saturation intensity is defined as

$$I_{sat} = \frac{h\nu}{\sigma\tau_u} \quad , \tag{3}$$

where h is Planck's constant, ν is the lasing frequency, σ is the stimulated emission cross section, and τ_u is the upper state lifetime. Based on Eqs. (1) and (2), it is clear that the parameters g_o, α, and I_{sat} are essential for determining the output of the dual-pass amplifier, given that the input and characteristics of the unpumped zones, window, and mirror are known.

The approach of M. Shaw[2] will be used to arrive at an expression for the saturation intensity as a function of the lasing mixture makeup, the rate constants for the deactivation of the upper lasing state, the radiative lifetime, and the pump rate.

The upper state lifetime can be expressed as

$$\frac{1}{\tau_u} = \frac{1}{\tau_r} + \frac{1}{\tau_c} \quad , \tag{4}$$

where τ_r is the radiative lifetime and τ_c is the change in τ_u due to collisional quenching. The quenching reactions considered here are

$$KrF^* + Ar + Ar \xrightarrow{k_5} ArKrF^* + Ar \quad , \tag{5}$$

$$KrF^* + Kr + Ar \xrightarrow{k_6} Kr_2F^* + Ar \quad , \tag{6}$$

$$KrF^* + Kr + Kr \xrightarrow{k_7} Kr_2F^* + Kr \quad , \tag{7}$$

$$KrF^* + e^- \xrightarrow{k_8} Kr + F + e^- \quad , \tag{8}$$

$$KrF^* + F_2 \xrightarrow{k_9} Kr + F + F_2 \quad , \tag{9}$$

and

$$KrF^* + Kr \xrightarrow{k_{10}} Kr + Kr + F \quad . \tag{10}$$

Based on the above equations for the collisional quenching, the saturation intensity can be expressed as

$$I_{sat} = \frac{h\nu}{\sigma}\left\{\frac{1}{\tau_r} + k_5[N_{Ar}]^2 + k_6[N_{Ar}][N_{Kr}] + k_7[N_{Kr}]^2 + k_8[N_{e^-}] + k_9[N_{F_2}] + k_{10}[N_{Kr}]\right\} \quad , \tag{11}$$

where the $N_{i's}$ are number densities for the species identified. To arrive at a reasonable estimate over the pump time of the amplifier, the F_2 concentration will be estimated at a point halfway through the pump duration. Again following Shaw[2], the electron density at the pump duration midpoint is estimated by making the ionization rate equal to the electron attachment rate to F_2.

$$\frac{P}{V_i} = k_{11}[N_{e^-}][N_{F_2}] \quad , \tag{12}$$

where P is the pump rate (W/cm^3) and V_i is the mixture ionization potential in eV. Using Eqs. (12) in (11) and employing the ideal gas equation of state for a temperature of 300 K, the expression for the saturation intensity becomes

$$I_{sat}\,(MW/cm^2) = \frac{3.038}{\tau_r} + 3.15 \times 10^{24}\left\{k_5[P_{Ar}]^2 + k_6[P_{Ar}][P_{Kr}] + k_7[P_{Kr}]^2\right\} + 9.78 \times 10^7\, k_9[P_{F_2}] + 9.78 \times 10^7\, k_{10}[P_{Kr}] + \frac{0.59\, k_8 P}{k_{11}\, V_i [P_{F_2}]} \quad . \qquad (13)$$

In Eq. (13) the pump rate is in (MW/cm^3), the ionization potential is expressed in electron volts, and the partial pressures are expressed in torr. The radiative lifetime will be taken as 6.5 ns, and the rate coefficients to be used are listed in Table I. For comparison purposes, the rate coefficients used in the Los Alamos kinetics code[3] and those recommended by Shaw[2] are also listed. The justification for using the values listed is that the agreement of the calculated I_{sat} values with values inferred from experiments is quite good, as can be seen in Fig. 2.

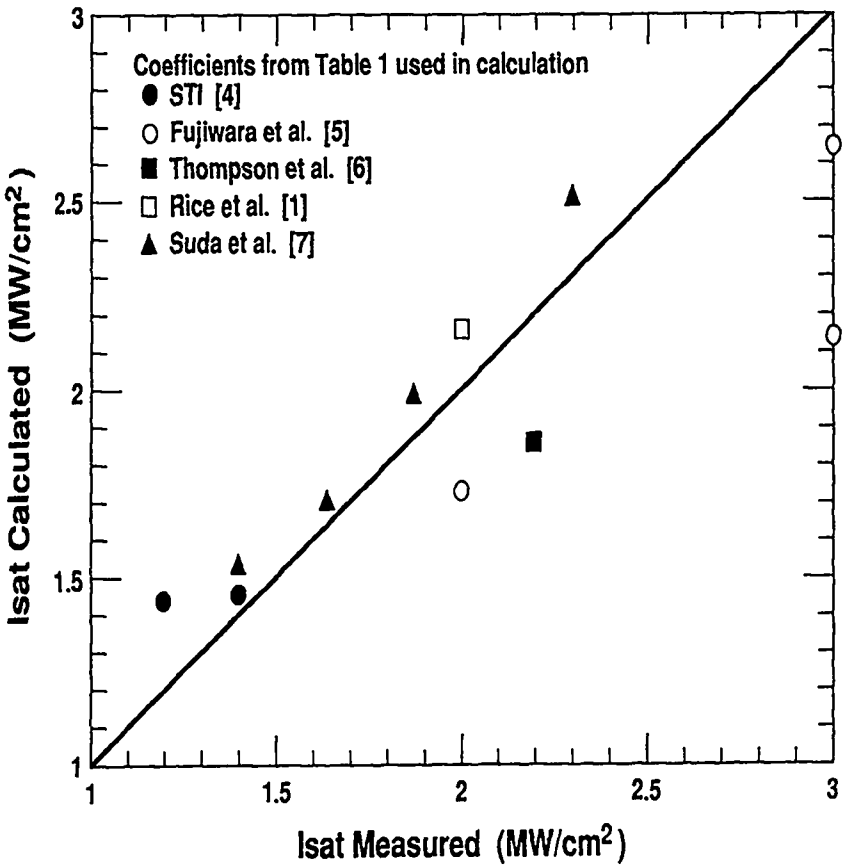

Fig. 2. The figure presents a comparison between I_{sat} inferred from experimental data and I_{sat} calculated using the rate coefficients recommended in Table I.

Table I

Rate Coefficients for Equation (13)

Source	τ_r(ns)	$k_5\left[\frac{cm^6}{sec}\right]$	$k_6\left[\frac{cm^6}{sec}\right]$	$k_7\left[\frac{cm^6}{sec}\right]$	$k_8\left[\frac{cm^6}{sec}\right]$	$k_9\left[\frac{cm^6}{sec}\right]$	$k_{10}\left[\frac{cm^6}{sec}\right]$	$k_{11}\left[\frac{cm^6}{sec}\right]$
M. Shaw	6.5	$8x10^{-32}$	$7x10^{-31}$	$7x10^{-31}$	$2.2x10^{-7}$	$8x10^{-10}$	NA	$2.3x10^{-9}$
Los Alamos (T-12)	6.7	$8x10^{-32}$	$6.5x10^{-31}$	$2.9x1^{-31}$	$1.0x10^{-7}$	$0.45x10^{-9}$	$2x10^{-12}$	$2.5x10^{-9}$
Recommended (Sullivan)	6.5	$8x10^{-32}$	$6.4x10^{-31}$	$2.5x10^{-31}$	**	$8x10^{-10}$	$2x10^{-12}$	$2.3x10^{-9}$

**$k_8 = \left[0.1\ (1 - \chi_{Kr})^2 + 2.7\ \chi_{Kr}^{1/5}\right] \times 10^{-7}$, where χ_{Kr} is the krypton mole fraction.

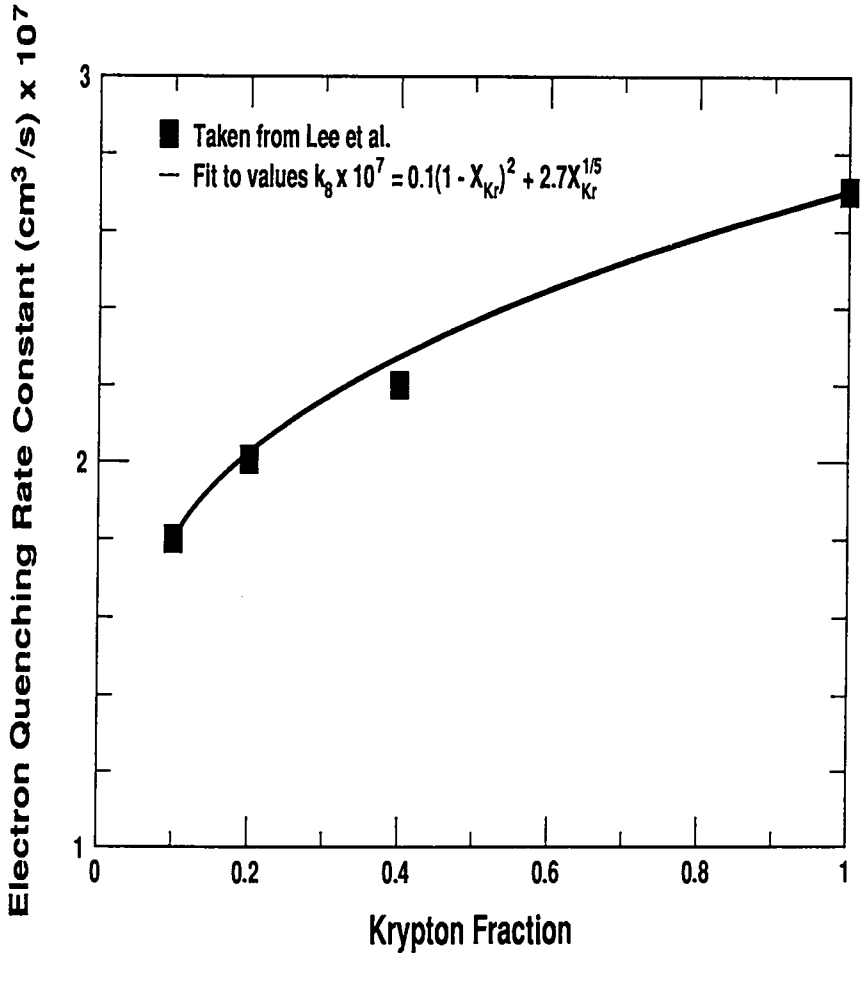

Fig. 3. The electron quenching rate in KrF lasers is a function of the krypton concentration. Shown is a mathematical fit to the data of Lee at al.[8]

The equation for the electron quenching rate coefficient shown in Table I was generated using values recommended by Lee et al.[8] based on best fitting the data of Suda et al.[7] Figure 3 shows the comparison between the equation for k_8 and the values recommended by Lee. A constant value for k_8 of 2.2×10^{-7} cm^3/s leads to good agreement between calculated and inferred values of I_{sat} for high krypton fractions but does not fit the low krypton fraction data as well.

The small signal gain is related to the formation efficiency, pump rate, and saturation intensity through the relation

$$g_o = \frac{\eta_f P}{I_{sat}} \quad . \tag{14}$$

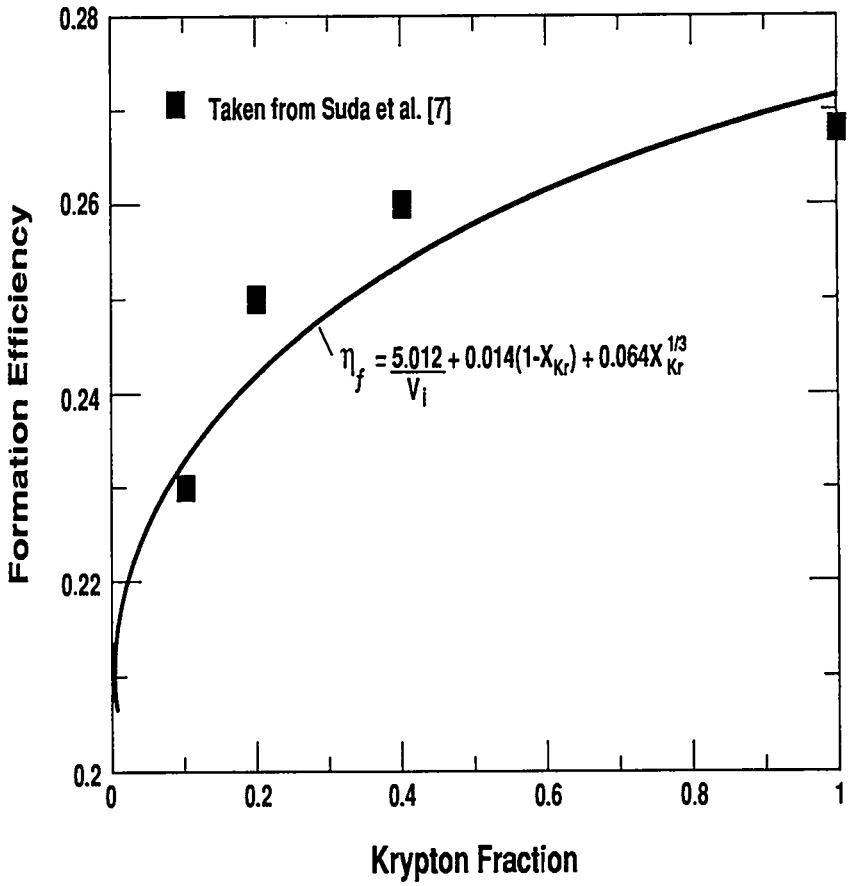

Fig. 4. The formation efficiency as a function of krypton concentration is presented in this figure. The data is that of Suda et al.[7] This figure illustrates why the original assumption by Shaw that the formation efficiency is nearly constant can be significantly in error for high krypton fractions.

Following Shaw[2], if one assumes ionization is the sole route to excitation and that the chemistry is 100% efficient, the formation efficiency can be approximated by

$$\eta_f = \frac{h\nu}{V_i} \quad , \tag{15}$$

where V_i is the mixture ionization potential. The formation efficiency in general depends on pump power and krypton fraction, so that Eq. (15) represents an approximation. A more accurate approximation can be arrived at by employing the data of Suda et al.[7] Figure 4 shows the experimental results and an approximate fit to the data,

$$\eta_f = \frac{h\nu}{V_i} + 0.014(1 - x_{Kr}) + 0.064 \times x_{Kr}^{1/3} \quad , \tag{16}$$

that gives reasonable agreement.

For the data of Suda et al.[7] a comparison between the calculated gain using Eq. (14) and measured gain for a range of krypton fractions and pump rates is shown in Table II.

Table II

Comparison of Calculated Gain to Data of Suda et al.[7]

Mixture F_2/Kr/Ar	Pump Rate MW/cm^3	Experimental g_o (%/cm)	Calculated g_o (%/cm)
0.4%/10%/89.6%	1.4	18.3	15.4
0.45%/20%/79.55%	1.64	18.5	15.5
0.50%/40%/59.5%	1.87	19.3	15.9
0.6%/99.4%/0%	2.3	20.6	18.7

The comparison shows that the calculation underestimates the gain by a small amount. The agreement is actually quite good, considering the simplicity of the calculational approach.

The final parameter needed for the model is the nonsaturable absorption. Thompson et al.[6] performed a survey of absorption data for KrF mixtures that reveals significant scatter in the data. Here we will follow the lead of M. Shaw[2] and divide the nonsaturable absorption into two parts, a pump-rate-dependent component and a component due to absorption in F_2. The pump-dependent portion arises from species such as Ar_2^+, Kr_2F, Ar_2^*, F^-, etc., and will be approximated by

$$\alpha_p = \frac{g_o}{12.5} \quad . \tag{17}$$

The fluorine-dependent part can be calculated using a value of 1.2×10^{-20} cm^2 for the absorption cross section of fluorine. The resulting expression for the nonsaturable absorption is

$$\alpha = \frac{g_o}{12.5} + 4.505 \times 10^{-4} P_{F_2} \quad , \tag{18}$$

where P_{F_2} is the partial pressure of F_2 in torr. Equation (18) is compared to the results of Klimek et al.[9] in Fig. 5 with the division between nonsaturable and saturable absorption taken to be 69% and 31%, respectively. The agreement gives confidence that Eq. (18) can be used for estimates of the nonsaturable absorption. It should be noted that the data of Klimek et al.[9] were for a krypton fraction of 4%, a fluorine pressure of 1.5 torr, and a total pressure of 1 atm.

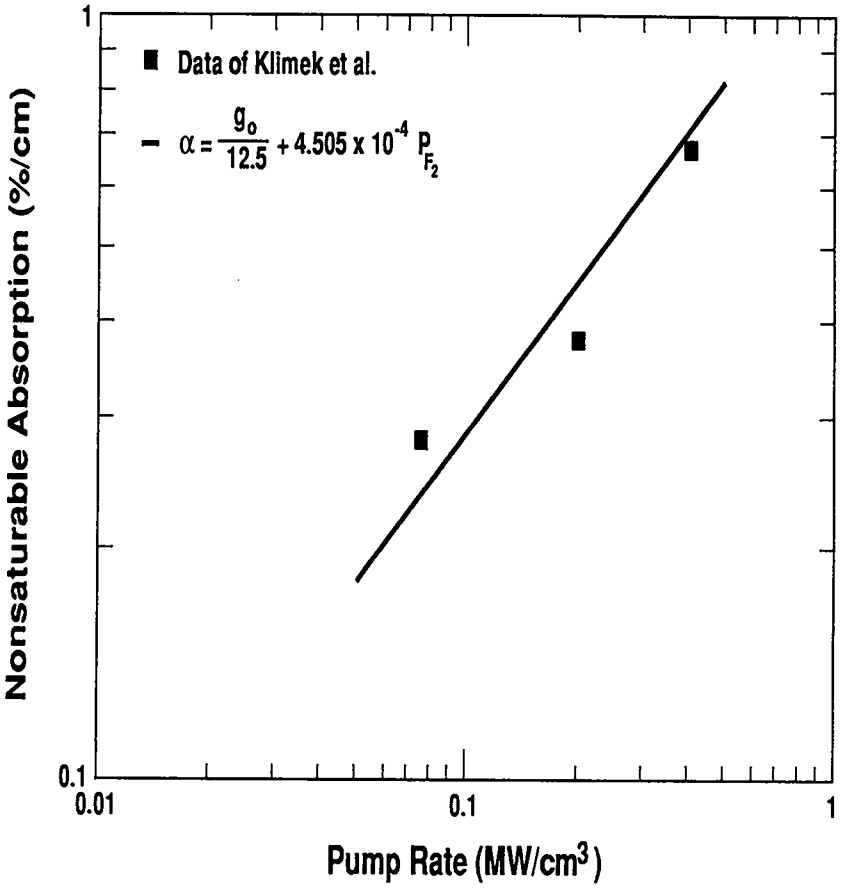

Fig. 5. The comparison of Eq. (18) to the data of Klimek at al.[9] shows that the use of this equation to calculate the nonsaturable absorption should give reasonable results over a range of pump rates from 50 to 500 kW/cm^3.

Fluorine Burn-up

To set the fluorine pressure for a given calculation we rely on the results of Rice et al.,[1] which show that maximum laser output can be maintained up to the point where the laser pump time is equal to the fluorine depletion time. The time to consume a charge of fluorine can be estimated by setting the disappearance of F_2 proportional to the formation rate of F^- where C is a constant and k is Boltzmann's constant.

$$\frac{dN_{F_2}}{dt} = -\frac{CP}{V_i} \quad , \tag{19}$$

or

$$\frac{dP_{F_2}}{dt} = -C\frac{kT}{V_i}P \quad , \tag{20}$$

The results of Klimek et al.[9] have shown that the proportionality constant is approximately 2, so that the burn-up time in ns is given by

$$t_b = 2.58\ V_i \frac{P_{F_2}}{P}\ , \qquad (21)$$

where P_{F_2} is the partial pressure of F_2 in torr and P is the pump rate expressed in MW/cm^3. For the design of large amplifiers the pump time is limited to 80% of burn-up and Eq. (21) is evaluated at the midpoint of the pump time to determine the required fluorine concentration.

Extraction Model

The extraction model adopted for the KrF design code is taken directly from the work of Rice et al.[7] They showed that the differential equation for the spatial variation of intensity could be integrated exactly to give a transcendental equation in terms of the product of the right-going and left-going intensities in the amplifier. The boundary conditions are modified to correspond to the geometry for a dual-pass amplifier as shown in Fig. 1. Reflection losses at the mirror and window and absorption losses in the unpumped end zones and internal to the window are included. The transcendental equation for $\delta = I_+ I_- = \text{Const}$ is solved by the Newton-Rapson method. Here, I_+ and I_- are the right and left propagating intensities in the amplifier. The method converges on a solution rapidly and is normally stable, provided the initial guess for δ is chosen as $4\ I_{in}$.

ASE Loss Estimation

To arrive at a reasonable estimate for ASE loss, the author examined 32 different amplifier calculation sets that were generated by W. Leland

of Los Alamos using a three-dimensional ASE code (see Reference 10, Chapter V, Section B). The calculation set was generated for a mixture of 50% Kr, 0.3% F_2 with the balance Ar at a total density of 1 Amagat. The relations,

$$g_o = P/5 \quad , \tag{22}$$

$$\alpha_{nsat} = 0.65\,(0.4 + P) \quad , \tag{23}$$

and

$$\alpha_{sat} = 0.35\,(0.4 + P) \quad , \tag{24}$$

where g_o, α_{nsat} and α_{sat} are in cm^{-1} when the pump rate P is in MW/cm^3, were used to arrive at values for the small signal gain and the nonsaturable and saturable absorptions. The side wall reflectivity (Rs) was assumed equal for the four sides of the laser cavity. The code used by Leland accounts for absorption loss in the unpumped gas in front of the end mirror and for the reflection loss at the end mirror. The calculated output does not include losses due to absorption in the dead space next to the output window or for reflections and absorption by the output window. All of the cases considered assumed uniform pumping in rectangular amplifiers with a width (w) in the electron propagation direction, a height (h), and a length (L) in the lasing direction. The results assume a 100% fill factor for extraction and a ratio of the upper state lifetime to the radiative lifetime of 0.366, which fixes the value of $I_{sat} = \frac{\tau_r}{\tau_u}\left(\frac{h\nu}{\sigma\tau_r}\right)$. The radiative lifetime is an easily measured quantity, whereas the upper lifetime is difficult to measure. The cases considered are summarized in Table III.

The ASE loss for each amplifier case listed in Table II was calculated for a full range of input intensities from 0.05 I_{sat} to 0.6 I_{sat} and for two

Table III

Amplifier Sizes and Pump Rates Used in ASE Calculations

Width (cm)	Height (cm)	Length (cm)	Pump Rate (MW/cm^3)
98	196	350	0.1
96	286	350	0.1
98	196	233	0.15
96	288	233	0.15
99	197	175	0.2
100	288	175	0.2
100	200	140	0.25
93	292	140	0.25
96	193	450	0.1
104	294	450	0.1
95	204	300	0.15
90	270	300	0.15
95	189	225	0.2
98	295	225	0.2
101	203	180	0.25
103	296	180	0.25

values of side-wall reflectivity (0.1 and 0.2). By plotting the ASE loss as a function of the dimensionless parameter

$$Su = G R_s \frac{wh}{L^2} , \qquad (25)$$

it was found that the results grouped closely when I_{in}/I_{sat} was used as a parameter. In Eq. (25), G is the amplifier stage gain in the absence of ASE losses. Figures 6a through 6e show the calculated ASE loss plotted for five values of I_{in}/I_{sat}.

The results shown in Fig. 6 can be fit using the mathematical expression

Fig. 6a-6d. Shown is the grouping of the calculated ASE loss values for the amplifier conditions listed in Table III as illustrated for various values of I_{in}/I_{sat}.

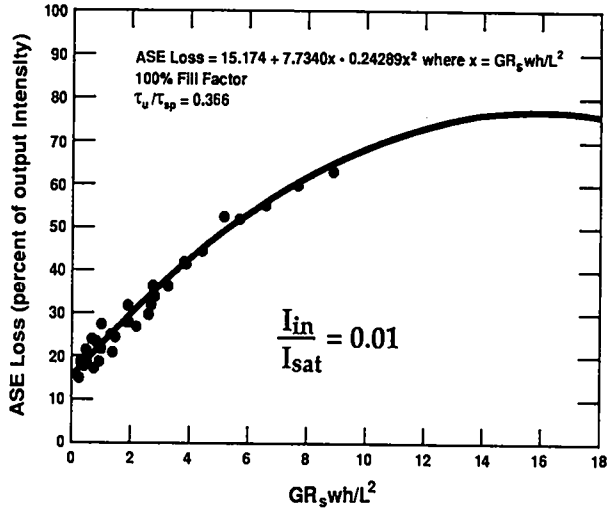

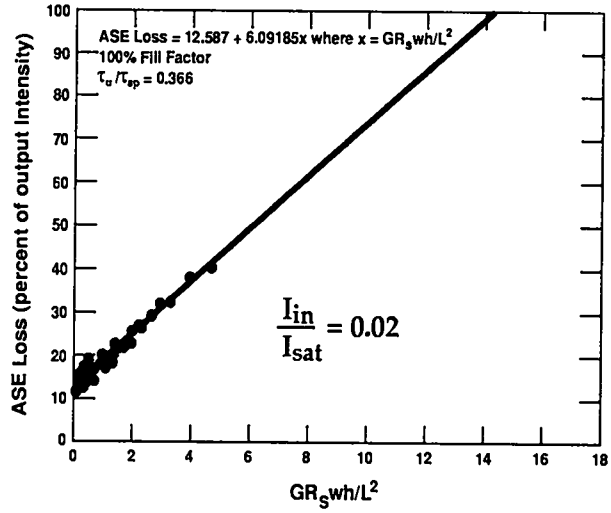

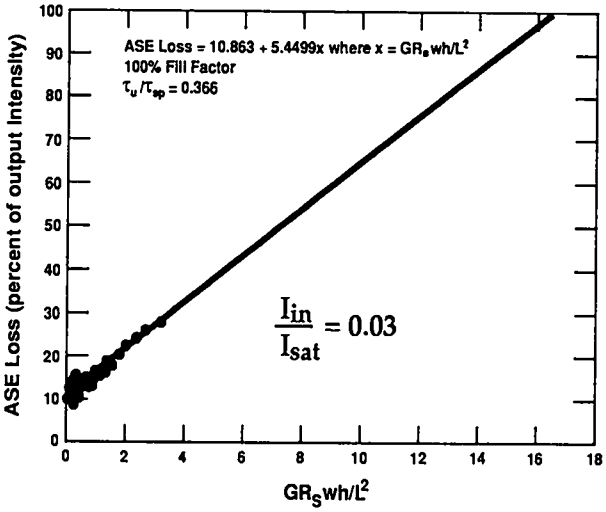

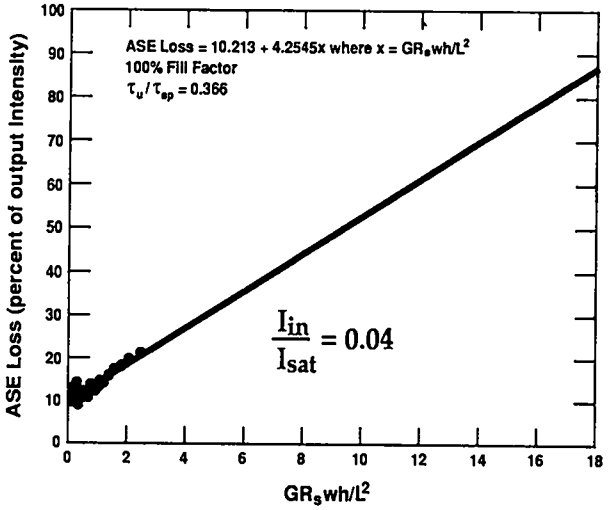

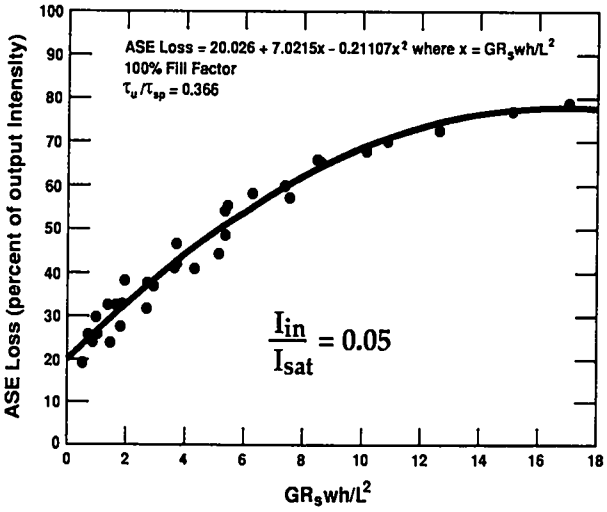

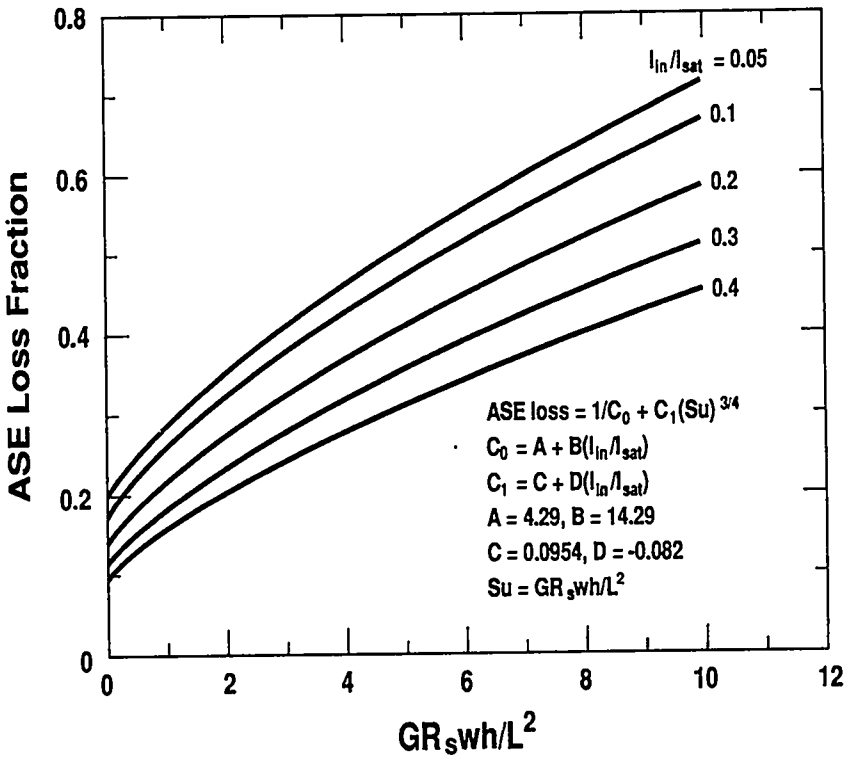

Fig. 7. Shown is a global approximation to the amplified spontaneous emission loss in large Krf amplifiers. The approximation will give answers that are normally within ±20% of Leland's[10] three-dimensional extraction.

$$ASE_{loss} = \frac{1}{Co} + C_1 (Su)^{0.75} \quad , \tag{26}$$

where the parameters Co and C_1 are functions of I_{in}/I_{sat} as explained in Fig. 7. The use of Eq. (26) gives a rapid estimation of ASE loss for large KrF amplifiers without resort to numerical models and is ideally suited for design calculations. It is apparent from Fig. 7 that a reasonable design criteria for limiting ASE loss is to assure that

$$\frac{GRs\ wh}{L^2} \leq 1 \quad . \tag{27}$$

This criteria will normally be satisfied for reasonable wall reflectivities (0.1 to 0.2) when the input intensity is 0.2 I_{sat} or greater.

Pumping Parameters

To provide an estimate of the voltage and current density needed to pump the laser from both sides, we use a straightforward approach of setting the pump power equal to the pump rate times the laser volume, or

$$2\,V\,J\,h\,L = \mathbf{P}\,w\,h\,L \quad . \tag{28}$$

Solving Eq. (28) for J gives

$$J = \frac{\mathbf{P}w}{2V} \quad , \tag{29}$$

where J is in A/cm^2 when **P** is the pump rate in MW/cm^3, w is the pumped width in cm, and V is the voltage in MV. The voltage or electron energy in eV required to pump a gas volume containing a mixture of argon and krypton can be estimated from data in Berger and Selzer[11] as

$$V = 0.0198[(1 + \chi_{Kr})\,p\,w]^{3/4} \quad , \tag{30}$$

where V is in MV when the gas mixture total pressure p is in atm and the pumped width w is in cm.

Scaling Considerations

The goal of ICF is to achieve capsule ignition and burn at high gain ($G \geq 100$) and to ultimately harness the energy release in a civilian power production system. A single-pulse laser facility would also have important applications for investigation of nuclear weapons physics and vulnerability and lethality studies. The proof of principle of ICF was carried out in underground tests at the Nevada Test Site by a joint team of scientists from Los Alamos and Livermore National Laboratories. Although these tests and those performed on the Nova laser at Livermore have served to bound the problem,

there is still a large uncertainty in the driver energy required to achieve high gain with an ICF capsule. A recent study by DOE[12] places the driver energy between 10 and 20 MJ for indirect drive and 6 and 12 MJ for direct drive. More recent calculations using highly shaped pulses and new target designs place the high gain region for indirect drive in the range of 2 to 6 MJ and about 1 to 2 MJ for direct drive. Regardless of the exact value of laser energy required, it is clear that current driver capabilities are a factor of 30 to 170 too low in energy. To approach MJ class drivers, one can either gang together a large number of small-to-moderate size amplifiers (20 to 100 kJ) or try to effect a solution with a small number of large amplifiers (250 to 500 kJ). At the present time no definitive comparison studies between these two approaches for electron-gun-pumped KrF lasers have been carried out.

For purposes of illustrating the interplay between the design parameters generated using a computer code based on the relations forwarded on the previous pages, we choose the point of view of using large KrF amplifiers. The relations governing the scaling to amplifiers as large as 500 kJ in output were forwarded by Ueda and Takuma.[13]

Performance Predictions for a Large KrF Amplifier

The amplifier for which we will calculate the performance and sensitivity to certain parameter variations has the characteristics and dimensions shown in Table IV.

Table IV

Large Amplifier Characteristics

Parameter	Value
Pumped length (m)	5.0
Width (m)	1.6
Height (m)	4.8
Unpumped zones each end (m)	0.2
Pump time (ns)	1080
Mirror reflectivity	0.98
Window reflectivity per surface	0.015
Window internal transmission	0.98
Operating pressure (atm)	1.0

Our objective will be to choose a pump rate, krypton fraction, input intensity, and side-wall reflectivity that will permit the amplifier to deliver 410 kJ with reasonable ASE loss and high intrinsic efficiency. The 410-kJ output must be achieved including the losses due to angular multiplexing of the extraction beams, losses due to amplification of reflected light from the output window, and losses due to baffling in front of the Hibachi foils that prevents build-up of parasitic oscillations. These added losses are estimated to be about 17%. Figure 8 shows the sensitivity of the amplifier performance to the amount of krypton in the laser mix at a pump rate of 190 kW/cm^3 and input intensity of 0.2 I_{sat}. From Fig. 8 it is clear that the intrinsic efficiency is a weak function of krypton fraction and that the required energy from the amplifier is achieved for a krypton fraction of about 0.8.

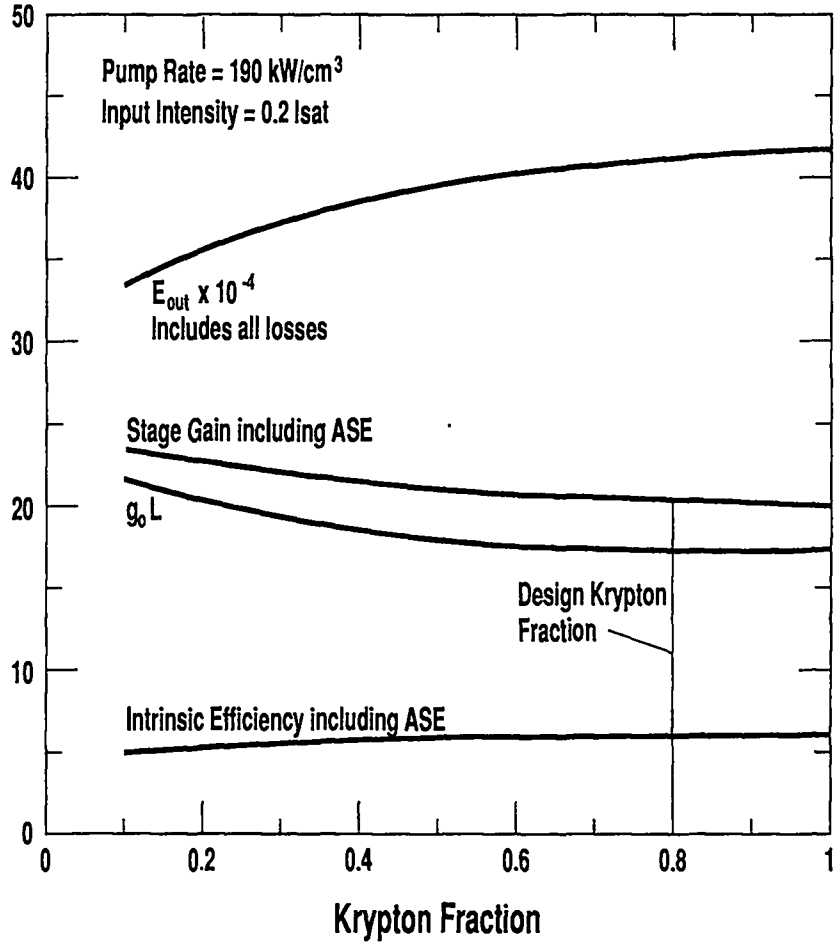

Fig. 8. Large KrF amplifier performance as a function of krypton fraction for a fixed pump rate and input intensity.

Figure 9 shows the variation of the amplifier performance with pump rate at a fixed krypton fraction of 0.8 and input intensity of 0.2 I_{sat}. Note that the intrinsic efficiency decreases as a function of pump rate and output of the amplifier is a strong function of pump rate. It is clear that one cannot simultaneously achieve intrinsic efficiencies near 10% and high energy output. As one increases the pump rate with the fixed conditions of Table IV of constant pump time and constant volume, the fluorine fraction must increase to permit achieving a fixed burn-up fraction of 80%. Thus, the absorption in the amplifier increases as the pump rate is increased, and consequently the intrinsic efficiency

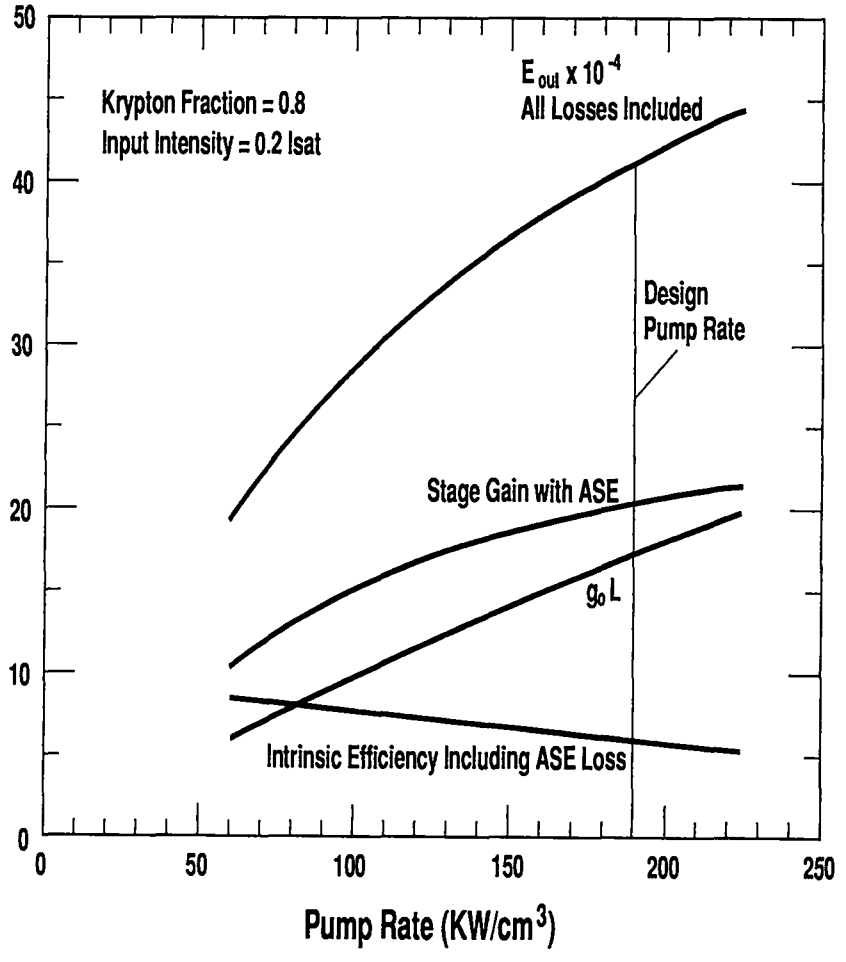

Fig. 9. Large KrF amplifier performance as a function of pump rate for a fixed pump time and input intensity.

decreases because the extraction efficiency decreases. One can conclude that the achievement of high intrinsic efficiency implies the use of low pump rates for large amplifiers with a subsequent energy penalty for a fixed pump time or the use of a longer extraction time to achieve more energy from the amplifier. The use of shorter pump times with high pump rates will also result in improved intrinsic efficiency for KrF amplifiers. To satisfy our desired energy output, a pump rate of 190 kW/cm3 is adequate for use of the amplifier in a single-pulse test facility where overall efficiency is not of paramount concern.

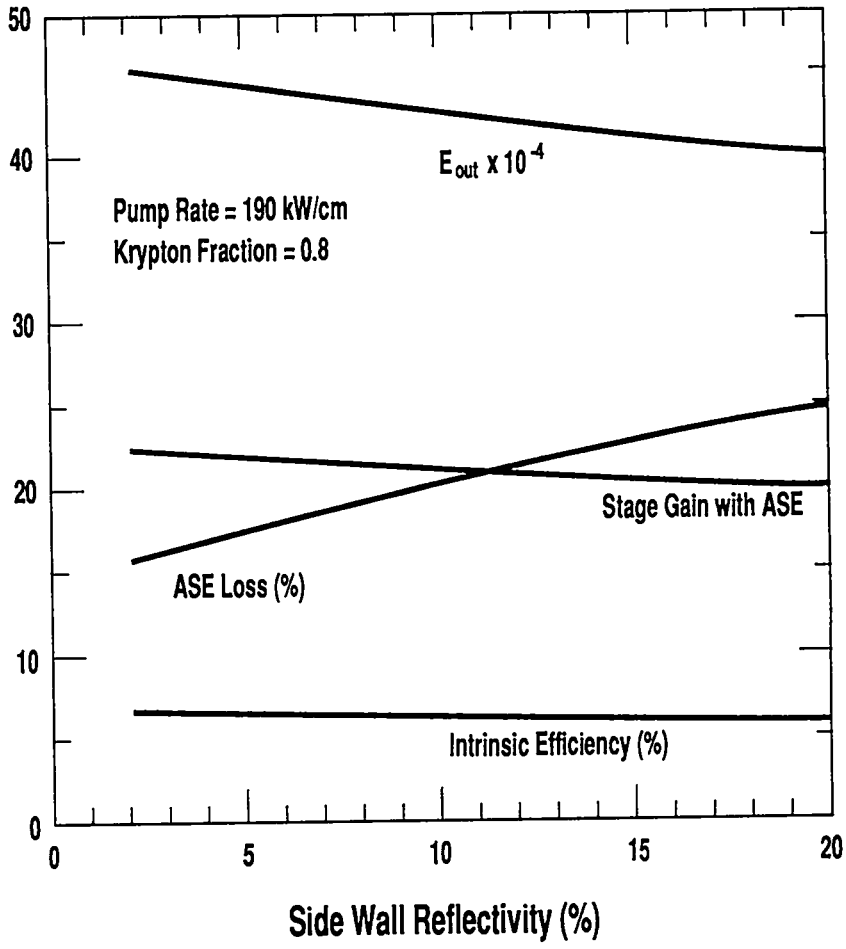

Fig. 10. Large KrF amplifier performance as a function of wall reflectivity for a fixed pump rate, fixed pump time, and 1 atm total pressure.

Figure 10 shows a plot of performance of the large amplifier as a function of side-wall reflectivity for a pump rate of 190 kW/cm^3 and a krypton fraction of 0.8. The effect of reducing the side-wall reflectivity is to reduce the losses due to ASE. Figure 10 shows that our desired performance of 410 kJ can be achieved at a side-wall reflectivity of 20%, but that significantly higher energy output could be achieved if the wall reflectivity could be reduced to 5%.

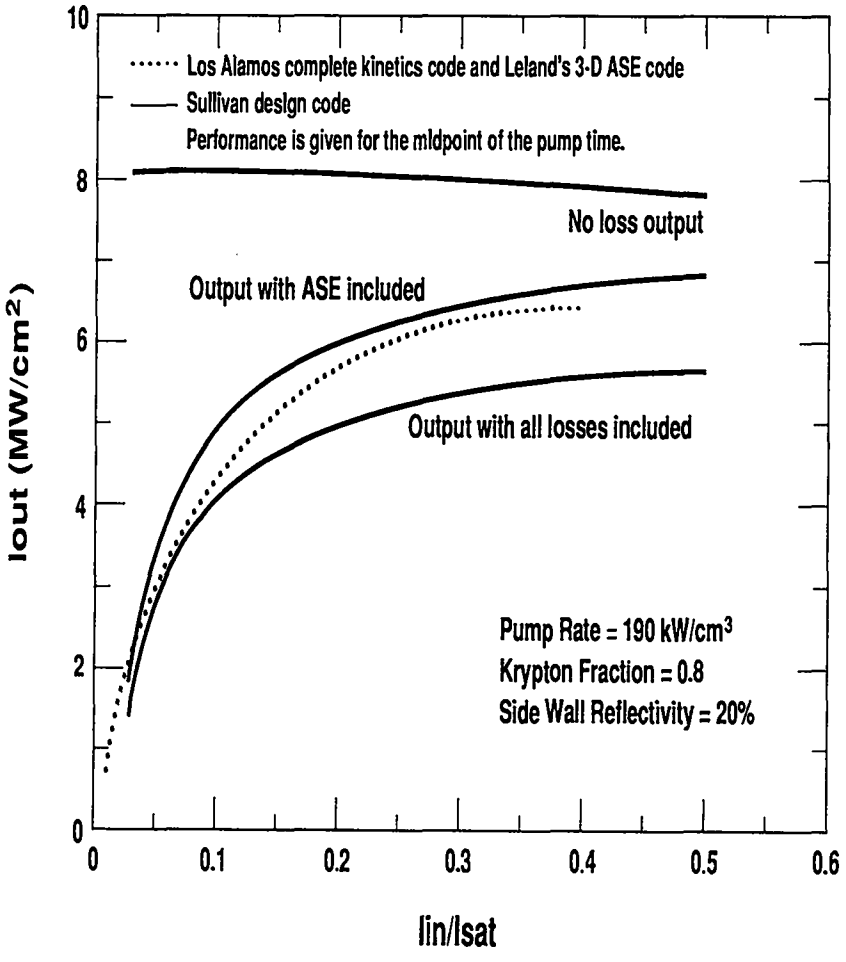

Fig. 11. Shown is a comparison between the predictions of the simplified KrF model presented in this paper and the calculations from the Los Alamos kinetics code coupled with Leland's[10] ASE code.

As a final comment on the performance of large KrF amplifiers, we show the performance for our selected amplifier as a function of input intensity for a fixed pump rate of 190 kW/cm^3, a krypton fraction of 0.8, and a side-wall reflectivity of 20% in Fig. 11. For comparison purposes, we show the calculated performance of the amplifier using the Los Alamos full kinetics code[3] and Leland's[10] 3-D extraction code that fully accounts for ASE losses. The agreement between the simplified design code and the more sophisticated codes is quite remarkable when one considers the degree of simplification that has been invoked.

Summary

The basis for a simplified KrF amplifier code that includes the controlling physics has been presented and shown to agree well with more sophisticated models. The code is particularly suited to design studies for single-pulse KrF fusion drivers where optimization of the amplifier chain requires numerous calculations of amplifier performance. The code is also applicable to the design of pulsed KrF amplifiers suitable for inertial fusion energy applications. ■

An Interparticle Collision Model for Electromagnetic Hybrid Simulations of High Density Plasmas

For further information on this subject contact:

Michael E. Jones

Vincent A. Thomas

Dan Winske

Los Alamos
National Laboratory
Los Alamos, NM 87545

Technical Review

Particle-in-cell methods have long been used to model collisionless plasma phenomena. At the other extreme, fluid methods have been used to model highly collisional plasmas. Hybrid models in which ions are treated by the particle-in-cell method and electrons are treated as a massless fluid allow one to ignore phenomena on the electron plasma frequency time scale and thus have proven to be useful for modeling certain aspects high-density plasmas. Until now particle collisions in PIC or hybrid models have been limited to scattering of the particles off a fixed background.

The key ingredient in developing plasma simulation methods that allow one to study the transitional region between collisional plasmas has been the development of an adequate interparticle collision model that takes into account the self-consistent reaction of the colliding species. We have developed and incorporated one type of interparticle collision model into the hybrid version of our particle-in-cell code ISIS.[1] The method is highly efficient and ensures local conservation of momentum and energy.

Monte Carlo Scattering Force

The main problem with a self-consistent scattering model in particle-in-cell code is the question of how to conserve momentum and energy locally. In the case of scattering from a fixed background, the reaction of the background is not

needed, so the usual random-number-based Monte Carlo scattering may be used. However, if we need the self-consistent scattering of two or more species, random scattering treating the scattering species as a fixed background will not conserve momentum and energy unless very large numbers of particles are used.

Another approach that has been suggested is to sort the particles and perform scattering in pairs to conserve momentum and energy. The sorting process can be time consuming and a prescription for which particles to pair together is not obvious. Molecular dynamics modeling uses this approach to describe the interactions. In general, particles are seldom exactly in the same location at a given time step, so a decision of when to scatter is not clear. Lattice gas algorithms solve this problem by requiring all the particles move at the same velocity.

The approach to collision modeling presented here is a natural extension of the particle-in-cell method. It involves defining a mesh quantity for the collision operator that can be viewed as a "collision field." This field will mediate the collision force and we will require that this force give local conservation of momentum and energy. Define $F_{a\beta}$ as the force on a particle in species α due to collisions with the particles of species β. Momentum conservation requires

$$\langle \mathbf{F}_{\alpha\beta} \rangle = - \langle \mathbf{F}_{\beta\alpha} \rangle \ , \qquad (1)$$

where the brackets denote distribution function averages. For example, the density, η_α and velocity, $\langle v_\alpha \rangle$ moments are given by

$$n_\alpha \equiv \int f_\alpha(v) d^3v \text{ and } \langle v_\alpha \rangle \equiv \frac{1}{n_\alpha} \int f_\alpha(v) v d^3v \ . \qquad (2)$$

We will also require that our collision force conserve energy locally:

$$\langle \mathbf{v}_\alpha \cdot \mathbf{F}_{\alpha\beta} \rangle = - \langle \mathbf{v}_\beta \cdot \mathbf{F}_{\beta\alpha} \rangle \ , \qquad (3)$$

Equations (1) and (3) represent conservation laws only in an average sense. If we perform the integral in Eq. (2) by weighted sums over the particles, these restrictions ensure that the first three moments of the distribution function (density, velocity, and temperature) are conserved. Note that we are not requiring microscopic (every particle) conservation laws. We will furthermore assume that the force is a function only of the first 3 moments and the particle velocity; i.e.,

$$\mathbf{F}_{\alpha\beta} = \mathbf{F}_{\alpha\beta}\left(n_\alpha, n_\beta, \langle \mathbf{v}_\alpha \rangle, \langle \mathbf{v}_\beta \rangle, \langle \mathbf{v}_\alpha^2 \rangle, \langle \mathbf{v}_\beta^2 \rangle, \mathbf{v}_\alpha\right) \qquad (4)$$

There are many possible choices of $\mathbf{F}_{\alpha\beta}$ that satisfy Eqs. (1) and (3). We have considered the following simple form of the collision force

$$\mathbf{F}_{\alpha\beta} = \nu_1 n_\beta \left(\langle \mathbf{v}_\beta \rangle - \langle \mathbf{v}_\alpha \rangle\right) + \nu_2 n_\beta \, \Delta T_{\beta\alpha} \left[\frac{\mathbf{v}_\alpha - \langle \mathbf{v}_\alpha \rangle}{\langle \mathbf{v}_\alpha^2 \rangle - \langle \mathbf{v}_\alpha \rangle^2}\right]$$

$$- \nu_3 n_\beta \left(\langle \mathbf{v}_\beta \rangle - \langle \mathbf{v}_\alpha \rangle\right) \times \mathbf{R} + \nu_4 n_\beta \left(\langle \mathbf{v}_\beta \rangle - \mathbf{v}_\alpha\right) \ , \qquad (5)$$

where the temperature difference $\Delta T_{\beta\alpha} \equiv m_\beta \left(\langle \mathbf{v}_\beta^2 \rangle - \langle \mathbf{v}_\beta \rangle^2\right) - m_\alpha \left(\langle \mathbf{v}_\alpha^2 \rangle - \langle \mathbf{v}_\alpha \rangle^2\right)$. The parameters ν_1, ν_2, ν_3, and ν_4, may depend only on the local moments. The vector $\mathbf{R}$ is generated from random numbers. We have not developed a first principles argument for this form of the force; rather, it was chosen from somewhat heuristic arguments. The first term provides a

drag due to the relative motion of the two species and corresponds to the Krook model used for fluid equations. The second term provides for temperature equilibration between the two species. The third term represents a scattering operator that on the average does not change the local momentum or energy. The last term is similar to the first and is added to ensure conservation of energy.

It is straight forward to show the momentum conservation as defined by Eq. (1) is satisfied by the force in Eq. (5) for an arbitrary choice of the parameters. The energy conservation equation, Eq. (3), places a constraint on the parameters which we write as

$$\nu_4 = \frac{-\nu_1 \left(\langle \mathbf{v}_\beta \rangle - \langle \mathbf{v}_\alpha \rangle \right)^2}{\langle \mathbf{v}_\alpha^2 \rangle + \langle \mathbf{v}_\beta^2 \rangle - 2 \langle \mathbf{v}_\alpha \rangle \cdot \langle \mathbf{v}_\beta \rangle} \tag{6}$$

The other parameters, ν_1, ν_2, and ν_3, are unconstrained. The first parameter is related to the rate at which momentum is exchanged, the second parameter is related to the rate at which the temperatures equilibrate and the last parameter is related to the rate of angular scattering. The scattering term is complicated by the fact that this term can also lead to momentum and energy exchange if the mean free path of the particles are large enough. A prescription for how to choose these parameters to model a given physical situation is still under investigation. In general the model, however, exhibits the correct behavior for the processes of momentum and energy exchange and scattering. It contains enough free parameters that most physical situations can be modeled.

It should be noted that there is nothing in the formalism that prevents the collision force from being applied to electron-ion collisions and/or self-collisions. In the hybrid model, the electrons are treated as a massless fluid. Therefore, the force on the electrons is the grid averaged force. Furthermore, the scattering term time averages to zero. In this limit only the first and last terms in Eq. (5) survive and the force on the electron fluid is

$$\langle \mathbf{F}_e \rangle = \sum_\beta \mathbf{F}_{e\beta} = \sum_\beta (\nu_1 + \nu_4) n_e n_\beta \left(\langle \mathbf{v}_\beta \rangle - \langle \mathbf{v}_e \rangle \right) \ , \tag{7}$$

which is of the same form as the usual Krook term.

Collisions for like particles within a species in this formalism do not exchange momentum and energy directly. For $\beta = \alpha$, the only term that survives is the third term in Eq. (5), or the scattering term

$$\mathbf{F}_{\alpha\alpha} = \nu_3 n_\alpha \left(\langle \mathbf{v}_\alpha \rangle - \langle \mathbf{v}_\alpha \rangle \right) \times \mathbf{R} \ . \tag{8}$$

The effect of this term is to provide a rotation of the distribution. This does not mean, however, that momentum and energy cannot be exchanged within a species. The exchange occurs through spatial mixing caused by the rotation.

Numerical Implementation

For computational convenience it is desirable to regroup the terms in Eq. (5) as follows

$$\mathbf{F}_{\alpha\beta} = \mathbf{F}^{(1)}_{\alpha\beta} + \mathbf{F}^{(2)}_{\alpha\beta} \mathbf{v}_\alpha + \mathbf{v}_\alpha \times \mathbf{N} \ , \tag{9}$$

where

$$\mathbf{F}^{(1)}_{\alpha\beta} \equiv (\nu_1 + \nu_4) n_\beta \langle \mathbf{v}_\beta \rangle - \left(\nu_1 + \nu_2 \frac{\Delta T_{\beta\alpha}}{\langle \mathbf{v}_\alpha^2 \rangle - \langle \mathbf{v}_\alpha \rangle^2} \right) n_\beta \langle \mathbf{v}_\alpha \rangle - \nu_3 n_\beta \langle \mathbf{v}_\beta \rangle \times \mathbf{R} \quad , \tag{10}$$

$$\mathbf{F}^{(2)}_{\alpha\beta} \equiv \left(\nu_2 \frac{\Delta T_{\beta\alpha}}{\langle \mathbf{v}_\alpha^2 \rangle - \langle \mathbf{v}_\alpha \rangle^2} - \nu_4 \right) n_\beta \tag{11}$$

and

$$\mathbf{N} \equiv \nu_3 n_\beta \mathbf{R} \quad . \tag{12}$$

In this form we can see that the first term is equivalent to an electric field and the last term is equivalent to a magnetic field. Thus, we can use the usual Boris particle pusher. We treat the term proportional to $\mathbf{v}_\alpha$ as an additional electric field term after the first half and before last half of the electric field update. These forces are in fact added as a separate gather operation on the particles. The velocity update takes place with both real fields and collision fields simultaneously.

Tests of the Method

As an example of the test of the collision mode, Fig. 1 shows the distribution function of two species interacting via our model. The particles are initialized as overlapping sphere in 2-D cylindrical (r-z) coordinates. The parameters are chosen so that equilibration occurs before much separation. ■

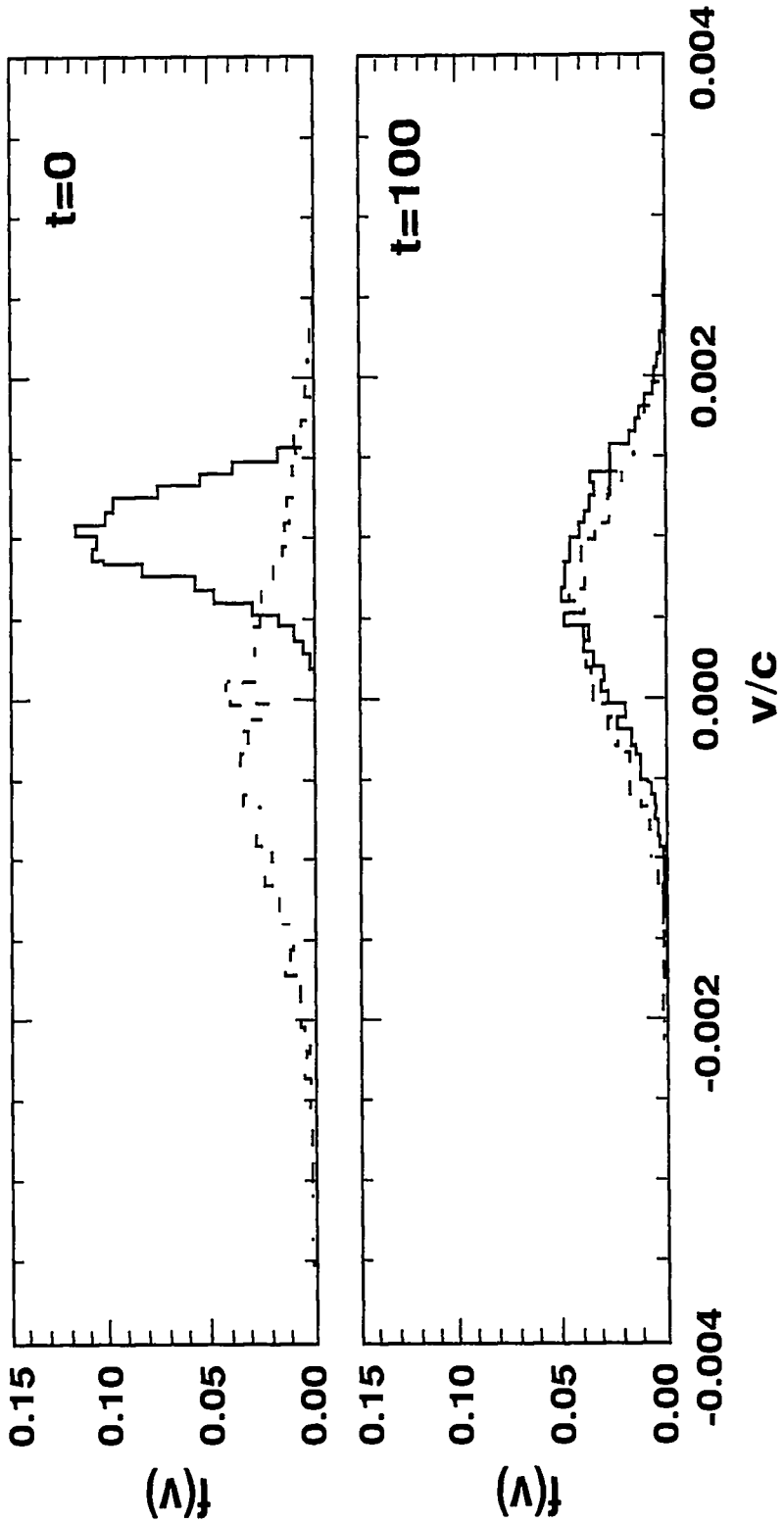

Fig. 1. Evolution of distribution functions for two colliding species in the absence of fields. The colder drifting Maxwellian equilibrates with the warmer stationary Maxwellian by exchanging momentum and energy.

BETA-LAYERING OF SOLID DEUTERIUM-TRITIUM IN A POLYCARBONATE SPHERE

For further information on this subject contact:

Jim K. Hoffer

John D. Simpson

Larry R. Foreman

Los Alamos
National Laboratory
Los Alamos, NM 87545

Abstract

We have examined several of the variables that affect the beta-layering process in which nonuniform layers of solid deuterium-tritium (DT) are driven toward uniformity by beta-decay induced sublimation. For these experiments, a 9 mm diameter polycarbonate spherical was partially filled with a 50-50 mix of DT liquid, frozen, and then held at 17 K. We measured the equilibration time constant τ as functions of solid layer thickness, ^{4}He exchange gas pressure, and age. Solid layer thicknesses ranged from 200 μm to 650 μm, exchange gas pressures from 0 to 600 torr, and age from 0 to 104 days. Results show a significant final solid layer anisotropy with exchange gas pressures above 5 torr, and τ values that increased with age by 0.01 min/day for 200-μm-thick layers, and by 0.5 min/day for 650-μm-thick layers. The time constant is shown to be a weak function of exchange gas pressure.

Introduction

The development of high-gain targets for inertial confinement fusion requires that the DT fuel layers exhibit a highly uniform profile. It has been demonstrated elsewhere[1,2,3] that a

nonuniform layer of solid DT can be driven toward uniformity by the process of radioactively induced sublimation (beta-layering). The tritium beta-decay produces temperature gradients[1] across the solid fuel layers that drive the sublimation of solid DT from thicker to thinner layers, forcing the layers toward uniformity. In previous work, the beta-layering process was studied in cylindrical geometry for both solid tritium[1] and solid DT layers[3,4] inside a high-thermal conductivity copper cell. The cell wall interior boundary was therefore nearly perfectly isothermal, resulting in very low values of the final solid layer anisotropy δ_∞. In contrast, the present experiments utilize a low thermal conductivity spherical cell, to simulate the low-Z plastic material and the actual geometry of prototype ICF reactor targets. If the thermal gradients in the ^{4}He exchange gas are not spherically symmetric, then observable values of δ_∞ could arise, with detrimental consequences to the ultimate target yield.

Aging simply implies the buildup of stagnant ^{3}He gas in the central vapor space, creating increasing resistance to DT vapor transport and thus causing the equilibration time constant τ to increase with time.[4] Using theoretical modelling, Giedt[5] has shown that when ^{3}He is present, then τ is also a function of both the cell wall thermal conductivity k_W and the heat transfer coefficient of the ^{4}He exchange gas h, which is pressure dependant.

Experimental Set-Up and Procedures

A detailed description of the experimental apparatus is given elsewhere[1,3], and will not be

repeated here. The major components are as follows: the DT gas handling system, including a palladium bed for storage and cleaning of the DT between experiments; a closed-cycle helium refrigerator-cooled cryostat; a multilayer containment system, providing tritium containment and a cryogenic environment for the DT target cell; a polycarbonate (PC) target cell with a stainless steel fill tube; and an imaging system including an incandescent backlighter, relaying optics, a CCD camera and a video frame grabber and image processing software. Data reduction and analysis were done using a 386 computer and several high-level software packages.

The PC cell is enclosed by a secondary containment cylinder which is filled with ^4He exchange gas at the desired pressure. Experiments were begun by filling the cell to the required level with DT liquid at 20 K, then quickly lowering the cell temperature to 17 K, about 2.8 K below the triple point. Figure 1 shows the sphere just after the initial freeze. Part of the DT liquid remains in the stainless steel fill tube and also freezes, providing a solid plug that prevents any further transport of DT in to or out of the cell. We developed a system to correlate initial liquid level to final uniform solid layer thickness d, based on the volume of the liquid relative to the volume of the cell. Between most experimental runs, the solid DT was liquified by shining an incandescent bulb into an orthogonal viewing port. This simple method maintained a constant fuel level and hence constant d from run to run because the solid plug in the DT fill tube remained frozen. Equilibration time constant, τ, and anisotropy, $\delta(t)$, were obtained by the following techniques.

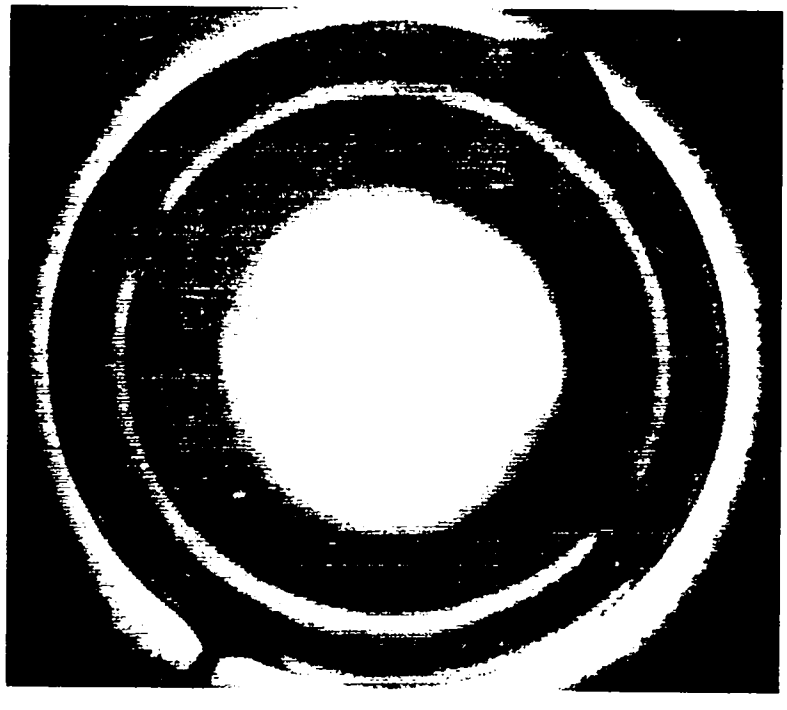

Fig. 1. A photograph of the clear spherical target cell filled ~20 % full with solid DT. This photo shows the cell just after the initial freeze, when the solid layer anisotropy is at its maximum. The solid is seen as an irregular clear (white) layer distributed along the bottom half of the interior of the cell. The stainless steel filling tube is near the bottom of the cell. A similar tube on the other side serves only to help in mounting the cell.

An image of a solid layer section was captured after focusing the optics at the vertical plane passing through the center of the PC shell (see Fig. 1). With the aid of an edge-tracing software routine, ~600 points were determined around the circumference at the inner wall of the PC shell (the shell wall - DT solid interface). The precise center of the PC shell was determined using a circle-fitting routine. The average value of the internal radius of the shell, R_i, then could be determined. Another series of points were defined along the inside of the solid layer (the DT solid-vapor interface). Thus, the radial distance between the center of the shell and the inner edge of the DT solid, as well as the thickness $d(\varphi)$ of the solid layer itself (by subtracting these values from R_i), was defined at 600 points along the 2π section. For a uniform solid layer,

Fig. 2. This photo shows the near-perfect uniform solid DT layer that results from beta-layering. The solid shows itself here as the inner clear (white) band. The central clear circular area is an out-of-focus image of the opal diffuser mounted behind the target in the secondary containment cylinder. The same diffuser shows up as the outermost clear band, now unaffected by the spherical optics of the target shell, but still out of focus.

$\delta = 0$, which means that $d(\varphi)$, as measured from the center of the sphere, is constant for $0 \leq \varphi \leq 2\pi$. For a nonuniform layer, $\delta(t)$ can be determined by taking the average value of $d(\varphi)$, then determining its standard deviation, or by doing a Fourier transform of $d(\varphi)$ as a function of φ. Images of the layering process were captured at regular time intervals during the equilibration runs. Figure 2 shows the PC sphere with the DT solid layer following equilibration. The values of τ and δ_∞ for each equilibration run were determined by taking the measured d(t) value for each time t and fitting the data to the general equation:

$$(1) \quad \delta(t) - \delta_\infty = \delta_0 e^{-t/\tau} \qquad (1)$$

where:

$\delta(t)$ = instantaneous solid layer anisotropy
δ_0 = initial anisotropy
t = time from initial freeze

Experiments and Results

1. Anisotropy vs exchange gas pressure

In our first set of experiments, we measured δ_∞ while varying the exchange gas pressure from 0.2 torr to 164 torr. The cell was filled with enough DT to yield a solid layer thickness of about 500 μm, and the cell temperature was maintained at 17.6 K. The data for these experiments is shown in Fig. 3. This graph shows large asymmetries at the higher exchange gas pressures, assumed to be the result of thermal

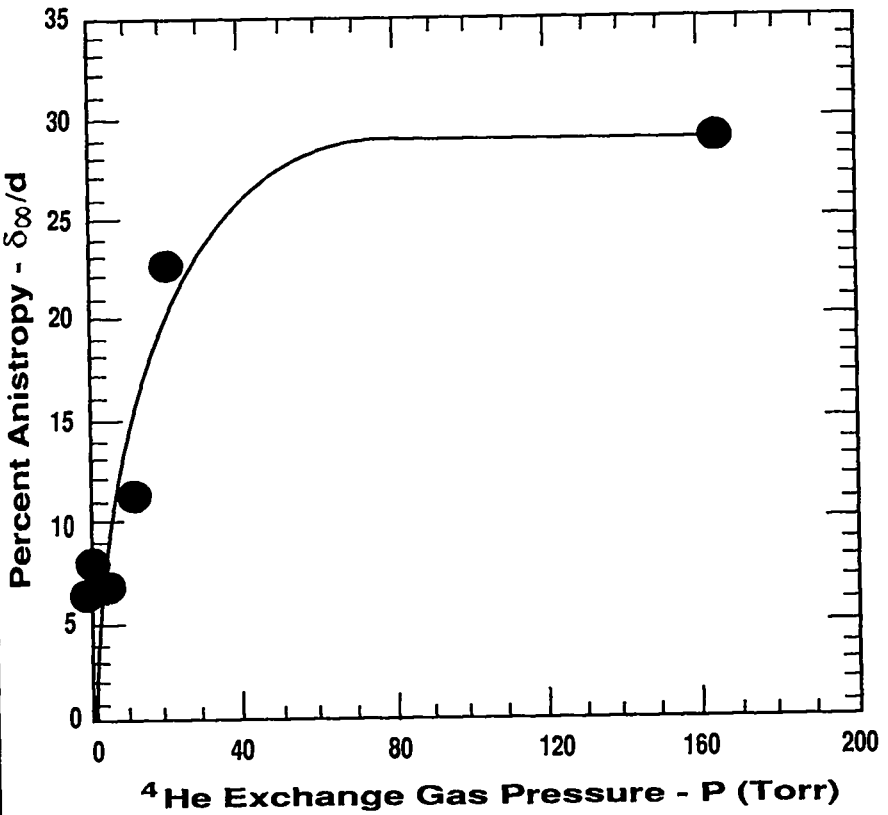

Fig. 3. Final solid layer anisotropy, δ_∞, expressed as a percentage of the total average thickness d, as a function of the ^{4}He exchange gas pressure. For these experiments, d was about 500 μm. The residual anisotropy at low pressure could be the result of heat-sinking effects of the cell fill and support tubes, aberrations in the optical system, or the limiting resolution of the imaging system.

convection in the ^{4}He exchange gas. As the pressure was reduced to 5 torr, the final asymmetry diminished to about 6%, where it leveled off. This residual asymmetry is probably due to the effects of the metal fill tube and support tube attached to the poles of the PC sphere. It could also be due to aberrations in the optical system or the limiting resolution of our CCD imaging system (640 x 480 pixel array).

2. Aging effect on the equilibration time constant

In the next series of experiments, shown in Fig. 4, we measured the effect of DT age on τ for two separate solid layer thicknesses. The

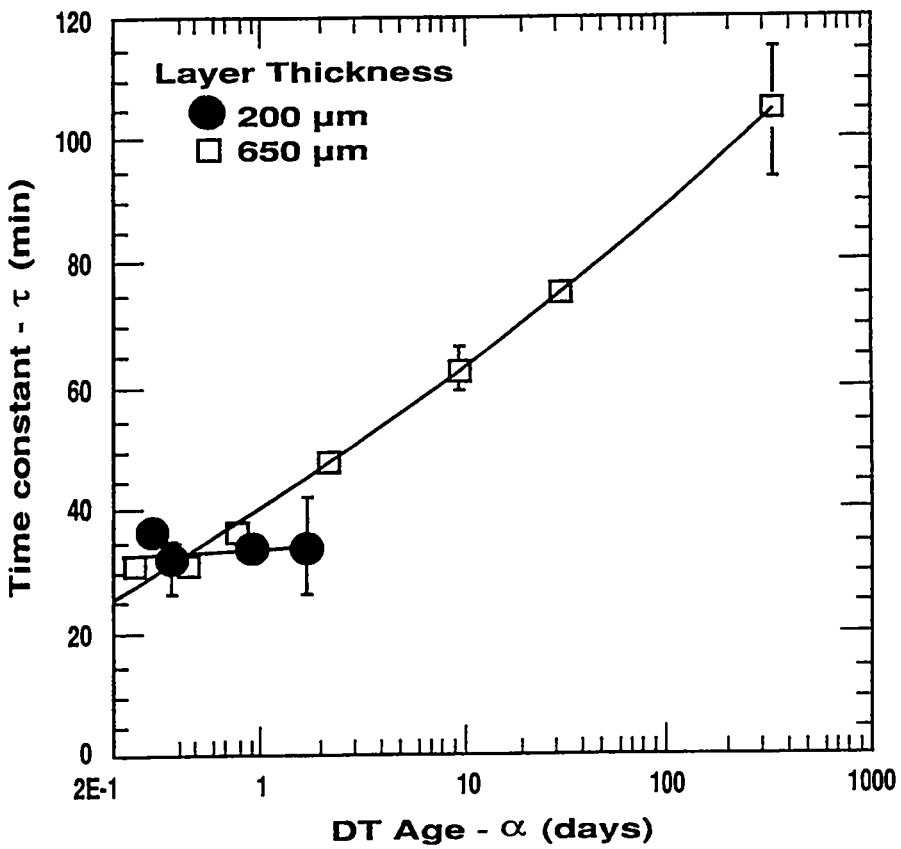

Fig. 4. The equilibration time constant τ vs the age a of the DT fuel in the target. Aging causes a buildup of stagnant ^{3}He gas in the central vapor space, which tends to impede the mass transfer of DT. The effect is more noticeable for the 650-µm-thick layer, where the overall rate of ^{3}He production is considerably faster. Each data set was fit to a second order polynomial with the results:

$\tau = 27 - .0092\,a + .0016\,a^2$ *(200 µm thickness), and*

$\tau = 21 + .477\,a + .0015\,a^2$ *(650 µm thickness).*

curve for the 200-μm-thick layer appeared relatively flat for the first 30 days, so we did not extend these experiments. The curve for the 650 μm layer began to show an observable rate of increase after 30 days so we elected to continue this experiment to 104 days in order to quantify the nature and size of the variation. The results of the latter experiment show a nearly linear increase in t of about 0.5-0.6 min per day. This is much lower than the 12 min/day measured previously[3] for the high-conductivity cylindrical copper cell. This is due to the differences in thermal shunting between high- and low-conductivity cell walls. When ^{3}He is present in the vapor space, DT mass transport occurs by diffusion[6] and a temperature gradient proportional to the concentration of ^{3}He is established. This is accompanied by a DT partial pressure gradient across the vapor space which is larger than would exist if no ^{3}He were present. In effect, the system responds to the impedance of ^{3}He by building up larger temperature and pressure gradients, and the overall rate is only slightly affected. However, in high-conductivity cells like the copper cylinder, the temperature gradient in the vapor space is partially shunted at the wall, reducing the equilibration rate drastically.[5] Additionally, the ^{3}He buildup rate in the vapor space was somewhat larger for the copper cylinder than for the spherical target because of the larger fraction of DT solid-to-cell volume in the cylinder experiments.[1,3,4] This effect is also responsible for the difference between the two sets of data in Fig. 4.

3. Time constant vs exchange gas pressure

A one-dimensional analysis of the beta-layering process in spherical geometries was performed by Giedt.[5] He examined the effects of varying the DT cell wall thermal conductivity and the ^{4}He exchange gas pressure on the equilibration time constant. We performed a set of experiments to measure the latter effect. These experiments were done by removing the ^{3}He from the DT between each run and refilling the Lexan sphere, producing "fresh" samples for each run. The exchange gas pressure was

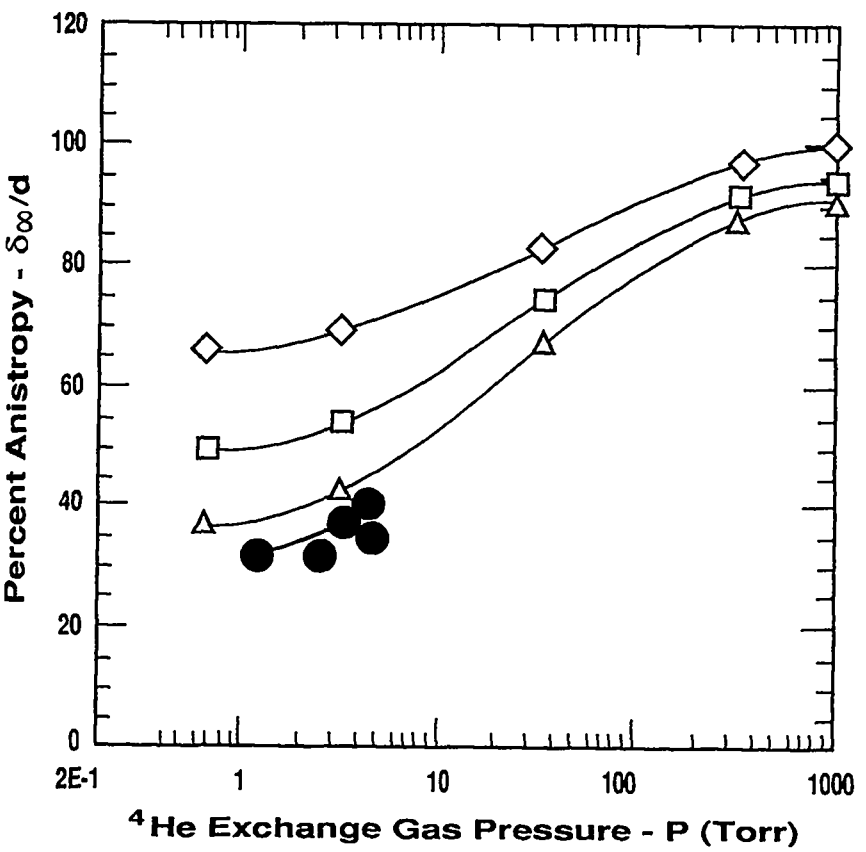

Fig. 5. The equilibration time constant τ as a function of the ^{4}He exchange gas pressure (converted to the equivalent heat transfer coefficient h to compare with the predictions of Giedt[5]). Giedt's calculations (open symbols) are for a 10-day-old sample and a 500-μm thick solid DT layer, whereas our data (closed circles) are for nearly fresh DT (zero age) and a 650-μm layer thickness. For the three predicted curves, target wall thermal conductivity increases vertically:
◇ - 0.001 W/cm K,
□ - 0.01 W/cm K, and
△ - 0.03 W/cm K.

set to the desired value before each fill and equilibration run. The ^{4}He pressures available to us limited the maximum h value to about 4.5. The results are shown in Fig. 5., along with the theoretical prediction made by Giedt. This graph is a rearrangement of Fig. 8. of Ref. 5 with ^{4}He exchange gas pressure converted to h. It shows the effects of h on τ for several values of wall thermal conductivity. Our data are for a PC sphere with a 650-μm solid layer and were taken at zero sample age. The Giedt curves are for slightly thinner solid layers (500 μm) and were generated for a sample age of ten days. Our data do fall within the range expected for the wall conductivity and sample age used and track the slope of the Giedt's predictions nicely. However, Giedt did not consider the case of zero age, at which the curves in Fig. 5 might all collapse to the ideal minimum rate constant of 26.6 minutes[1]. Thus our data show only that τ is a relatively weak function of the ^{4}He exchange gas pressure when no ^{3}He is present.

Conclusions

There are striking differences in the details of beta-layering occurring within low-conductivity polycarbonate walls, as opposed to high-conductivity copper walls as observed previously.[1,3,4] The most noticeable effect is the large amount of final anisotropy. This effect decreases as the pressure in the ^{4}He exchange gas is lowered, reaching a minimum below ~5 torr, which suggests that it is due to thermal convection. Maintaining adequate cooling with purely conductive heat transport, which occurs at pressures below ~2 torr, should not present a

problem for the target sizes of interest to ICF applications. However, whether the final anisotropy can be reduced to meet the stringent conditions required for laser-driven implosions is still an open question.

The effect of DT age (^{3}He content) on the equilibration rate in a polycarbonate shell is almost nonexistent, in contrast to the strong effect observed in copper. For practical ICF targets, the effect will not be significant unless the DT is very old.

Finally, the fact that these observations are in excellent agreement with computer modelling predictions by Giedt[5] and others[2-6] shows that our theoretical understanding of the beta-layering phenomenon is adequate. ■

Policy on ES&H

Implicit in all of our work is a respect for the health and safety of ourselves and those around us and an appreciation for the need to protect the environment in which we are privileged to work.

9. Klimek, D. E., Hsia, J. H. Jacob, J. H., Trainor, D. W., Duzy, C., and Hyman, H. A., "Kinetic Issues for Short-Pulse KrF Laser Operation," IEEE J. of Quantum Electronics, Vol. QE-17, 1847-1855 (1981).

10. Leland, W. T., "Amplified Spontaneous Emission in KrF Amplifiers," LA-UR-89-2675 Vol. II, Los Alamos National Laboratory (September 1989).

11. Berger, M. J., and Selzer, S. M., "Tables of Energy Losses and Ranges of Electrons and Positrons," NASA report No. Sp-3012 (1964).

12. "U.S. DOE Laboratory Microfusion Capability Study, Phase I Summary," U.S. DOE report DOE/DP-0069 (1989).

13. Ueda, K., and Takuma, H., "Scalability of High Power KrF Lasers for ICF Drivers," International Symposium on Short Wavelength Lasers and Their Applications," Springer Verlag (1988).

"An Interparticle Collision Model for Electromagnetic Hybrid Simulations of High Density Plasmas"

1. M. E. Jones, V. A. Thomas, R. J. Mason and D. Winske, "A Fully Electromagnetic Hybrid Model for High Density Plasma Simulations," Proceeding of the 13th Conf. on the Num. Sim. of Plasmas, PMA15, Santa Fe, NM, Sept. 17-20, 1989.

"Beta-Layering of Solid Deuterium-Tritium in a Polycarbonate Sphere"

1. J. K. Hoffer and L. R. Foreman, Phys. Rev. Lett. 60, 1310 (1988).
2. A. J. Martin, R. J. Simms, and R. B. Jacobs, J. Vac. Sci. Technol. A6, 1885 (1988).
3. J. K. Hoffer and L. R. Foreman, J. Vac. Sci. Technol. A7, 1161 (1989).
4. J. K. Hoffer, L. R. Foreman, J. D. Simpson, and T. R. Pattinson, Physica B 165&166, 163 (1990).
5. W. H. Giedt, LLL Report ENE 90-064 (1990).
6. T. P. Bernat, E. R. Maypoles, and J. J. Sanchez, Lawrence Livermore National Laboratory Inertial Confinement Fusion Quarterly Report, 1, 57 (1991), UCRL-LR-105821-91-2.

FOR FURTHER INFORMATION, CONTACT:

Stephen M. Younger
Program Director, ADNWT/ICF
MS E527
Los Alamos National Laboratory
Los Alamos, NM 87532
(505) 667-5167

This document was produced on a Macintosh II™, Varityper VT600P™, and Cannon™ Scanner using Microsoft Word™, Expressionist™, Adobe Illustrator™, and Pagemaker™.

Compiled, edited, and produced by Liz Courtney.

LALP-91-72
January 1992